JGR Atmospheres

Key Points:
- Lidar observations from above cloud layers significantly undercount the occurrence of mixed phase clouds over the Southern Ocean (SO)
- A latitudinal gradient in mixed-phase clouds is found associated with the Antarctic Polar Front of the Antarctic Circumpolar Current
- Current parameterizations that modify the phase detrainment temperature of shallow convection are not supported by observations. An alternate parameterization developed from SO surface data is suggested

Correspondence to:
G. G. Mace,
jay.mace@utah.edu

Mixed-Phase Clouds Over the Southern Ocean as Observed From Satellite and Surface Based Lidar and Radar

Gerald G. Mace[1] , **Alain Protat[2,3]** , **and Sally Benson[1]**

[1]Department of Atmospheric Sciences, University of Utah, Salt Lake City, UT, USA, [2]Australian Bureau of Meteorology, Melbourne, VIC, Australia, [3]Australian Antarctic Partnership Program, Institute for Marine and Antarctic Studies, University of Tasmania, Hobart, TAS, Australia

Abstract This study investigates the occurrence of mixed-phase clouds (MPC, i.e., cloud layers containing both liquid and ice water at sub-freezing temperatures) over the Southern Ocean (SO) using space- and surface-based lidar and radar observations. The occurrence of supercooled clouds is dominated by geometrically thin (<1 km) layers that rarely contain ice. We diagnose layers that are geometrically thicker than 1 km to contain ice ~65% and ~4% of the time from below by surface remote sensors and from above by orbiting remote sensors, respectively. We examine the discrepancy in MPC occurrence statistics as diagnosed from below and above the cloud layer. From above, we find that MPC occurrence has a gradient associated with the Antarctic Polar Front near 55°S with a rare occurrence of satellite-derived MPC south of that latitude. In contrast, surface sensors find ice in 33% of supercooled liquid water layers. We infer using observing system simulation experiments and data analysis that space-based lidar cannot identify the occurrence of MPC except when secondary ice-forming processes operate in convection that is, sufficiently strong to loft ice crystals to cloud tops. We conclude that the CALIPSO phase statistics of MPC have a severe low bias in MPC occurrence. Based on surface-based statistics in the SO, we present a parameterization of the frequency of MPC as a function of cloud top temperature that differs substantially from that used in recent climate model simulations.

Plain Language Summary The existence of snow in predominantly liquid clouds has important implications for the amount of sunlight absorbed mostly at the sea surface over the high latitude oceans. Particularly over the Southern Ocean, where satellite measurements suggest that ice concentrations are low, knowledge of how often clouds are snowing has critical climate implications. Observations from the surface have high fidelity in identifying snow below cold clouds. We use new measurements collected from Australian research vessels to establish an accurate survey of snow occurrence. We find that the occurrence of snow below cold clouds is much higher from ship observations than inferred from satellite. We explore reasons for this discrepancy and settle on an explanation that the low concentrations of ice-nucleating aerosol particles result in low concentrations of ice particles except where convective motions are strong enough to create ice particles spontaneously by freezing large drops. We provide a simple temperature-based parameterization of snow occurrence using surface-based measurements for atmospheric models to use.

1. Introduction

The occurrence of ice in subfreezing (hereafter supercooled) liquid phase clouds exerts significant controls on the energy balance of the Southern Ocean (SO; Bodas-Salcedo et al., 2016, 2019; Trenberth & Fasullo, 2010). The SO surface energy balance influences phenomena ranging from large-scale ocean circulation to large-scale atmospheric circulations. This includes the sequestering of carbon and heat (W. Liu et al., 2018; Marshall & Speer, 2012) in the ocean. In the atmosphere, the hemispheric distribution of precipitation is a direct response to the strength of the meridional thermal gradient (Cai et al., 2011; Ceppi & Hartmann, 2015) that is sensitive to the net sunlight absorbed at the ocean surface.

Because the vapor pressure over ice is less than that over water in the terrestrial atmosphere, liquid droplets at subfreezing temperatures are unstable in the presence of ice crystals. This instability causes rapid growth of ice particles at the expense of liquid-phase cloud droplets (Bergeron, 1935; Findeisen, 1938;

Methodology: Gerald G. Mace, Sally Benson
Project Administration: Gerald G. Mace, Alain Protat
Resources: Gerald G. Mace, Alain Protat
Software: Gerald G. Mace, Sally Benson
Supervision: Gerald G. Mace
Validation: Gerald G. Mace
Visualization: Gerald G. Mace, Sally Benson
Writing – original draft: Gerald G. Mace
Writing – review & editing: Gerald G. Mace, Alain Protat

Wegener, 1911). Because liquid droplets form on numerous cloud condensation nuclei relative to sparse ice-active nuclei (hereafter INP for ice nucleating particles) in supercooled clouds (Fossum et al., 2018; McCluskey et al., 2018), the ice that does form tends to precipitate, thereby depleting clouds of liquid water. Cloud dissipation through glaciation reduces cloud areal coverage with a concomitant impact on regional albedo (Vergara-Temprado et al., 2018). Reduced lower cloud cover then exposes the surface ocean to solar radiation that would otherwise have been reflected. The current thinking is that atmospheric models have been too aggressive in forming ice precipitation in SO clouds, resulting in high biases in absorbed sunlight. Becuase of the cloud cover biases, the simulated meridional temperature gradient that occurs in response to incorrect surface heating in the SO tends to be misplaced and weaker than observed. Errors in the meridional temperature gradient induce a cascade of other biases that range across weather and climate space and time scales (e.g., Schneider & Reusch, 2015).

The recent study of Schneider et al. (2020) exemplifies the far-reaching implications of the cloud phase in SO clouds. Using the most recent version of the Community Earth System Model (CESM, Hurrell et al., 2013), Schneider et al. (2020) implement a modification to the parameterization of shallow convective clouds that causes those clouds to detrain liquid water instead of ice to lower temperatures. First implemented by Kay et al. (2016) and further evaluated by Frey and Kay (2018), this seemingly minor change results in higher SO cloud cover and a large reduction of the absorbed shortwave bias by a factor of ~4. When coupled with natural stratospheric ozone loss, the CESM with the modified cloud parameterization replicates more accurately the observed poleward shift in the mid-latitude westerly jet. The jet stream's increased intensity then increases precipitation over the Antarctic ice sheets by a factor of ~3 compared to results from the same model without the changed cloud parameterization.

Observational studies of the absorbed shortwave bias over the SO have focused on the occurrence frequency of ice-phase precipitation (Bodas-Salcedo et al., 2016; Naud et al., 2014). Satellite data have provided the only broad observations of SO clouds in space and time, although recent shipborne studies have begun to fill in essential gaps (Fossum et al., 2018; Mace & Protat, 2018; Mace et al., 2021; Protat et al., 2017). In particular, the CALIPSO (Winker et al., 2009) and CloudSat (Stephens et al., 2008) satellites have significantly expanded our measurements that address SO cloud phase. CALIPSO can infer the cloud thermodynamic phase using depolarization when ice crystals contribute significantly to the volume integrated backscattered laser light. This capability is always limited to the first three optical depths from the cloud top. We have recently reimagined the algorithm that identifies the presence of ice in liquid-dominant clouds at subfreezing temperatures (hereafter mixed-phase clouds or MPC) from CALIPSO data by providing a physical basis for the choice of thresholds where depolarization ratios of backscattered laser light become inconsistent with single-phase liquid clouds (Mace et al., 2020). In this study, we expand upon Mace et al. (2020) to further explore the geographic and seasonal distributions of MPC over the SO and their association with oceanographic thermal boundaries. We then critically assess the impact of the geometry of observations (looking from above or below cloud layers using satellite and ship observations) on the statistical properties of MPC occurrence.

2. Method and Data Used

This study uses data from the Calipso and CloudSat satellites and measurements from ship-based depolarization lidar. The surface data were collected during three recent voyages into the SO by Australian research vessels. Because the lidar signal fully attenuates beyond optical depth ~3, views of cloud layers from above and below potentially provide very different information about the mixed-phase processes that may be ongoing in a cloudy profile. SO boundary layer clouds typically have optical depths >3 (Mace et al., 2021). Furthermore, the volume integrated backscatter at lidar wavelengths depends on the relative contributions of the hydrometeors. If the total cross-sectional area of ice crystals is small relative to that of the water droplets, the ice phase's presence may not be detectable. Therefore, it is uncertain whether layers observed from above that appear to the lidar as being entirely liquid phase may have ice in the column that is not sensed by the spaceborne lidar.

On the other hand, surface lidars can sense below the liquid cloud base for the presence of precipitating ice crystals that have fallen from the primarily liquid cloud layer. Because ice grows rapidly to large sizes and

precipitates, observing from the surface provides unambiguous evidence that mixed-phase processes have been or are ongoing in a cloud layer. In the overwhelming majority of cases, when sub cloud ice precipitation is observed, the cloud layer base shows no evidence of the ice phase precipitation in the depolarization ratio. This is because the water droplets that are typically several orders of magnitude more numerous than the ice crystals dominate the cloud base's light scattering process. We consider the presence of ice below the cloud base as evidence that the layer is mixed-phase. Because the lidar typically attenuates within a few tens of meters above cloud base when looking from below, we do not attempt to determine where in the layer the ice is present or whether it is present at cloud top.

In 2016 and 2018, the Research Vessel (RV) Investigator collected data from a 355 nm lidar system in campaigns called CAPRICORN I and CAPRICORN II see Royer et al. (2014) and Mace and Protat (2018) for a brief description of the RMAN lidar system and the CAPRICORN I campaign, while Mace et al. (2021) describe CAPRICORN 2. CAPRICORN 1 took place in March and April 2016 and went as far south as 53°S. During CAPRICORN II, data were collected as far south as the seasonal ice edge during January and February 2018 near 66°S. We also use data from a 532 nm micropulse lidar system from the MARCUS campaign (McFarquhar et al., 2021) that collected data from the RV Aurora Australis from November 2017 through March 2018. We only use MARCUS data collected between early January and March 2018 due to insufficient quality lidar data collected earlier.

Mace and Protat (2018) and Mace et al. (2021) describe the method used to identify MPC occurrence from the surface-based data. By examining warm layers where ice is not possible and ice-only layers, such as snow below cloud base, we identify the depolarization ratio threshold that separates ice hydrometeors from water droplets. The value we use to separate ice from liquid is a depolarization ratio of 0.03. The study by Haarig et al. (2017) shows that the depolarization ratio of sea salt aerosol is a strong function of humidity. At low humidity (below 50%) dried sea salt can have depolarization ratios in the 0.1 range. However, since we are considering cloudy environments, we can reasonably assume that the humidities in the sub cloud region are likely at least near ice saturation or ~80% with respect to water. This is in agreement with the radiosonde data that we have examined (Mace et al., 2021). For humidities in excess of 60% with respect to liquid, the depolarization ratio of sea salt aerosol is much less than 0.03 (Haareig et al., 2017; their Figure 12). We arrived at the original 0.03 value empirically by examining the depolarization ratios of warm cloud bases but that value of depolarization ratio is in general agreement with Haarig et al. (2017) results in the presence of humidified sea salt aerosol. We have tested the threshold for ice and found that there is no qualitative difference in our results between a value of 0.03 and 0.15. Nearly all volumes with certain ice, have depolarization ratios in excess of 0.1. For layers with subfreezing cloud base temperatures, we reason that because ice hydrometeors grow quickly to large sizes, they would precipitate into the layer below a liquid cloud base. Therefore, we look for precipitation from coincident W-Band radars in the 100 m layer below the cloud base. If the lidar depolarization ratios in the precipitation are consistent with ice, we label the cloud as mixed-phase. Otherwise, we label the cloud as liquid phase. This method of examining the phase of sub cloud precipitation cannot be applied to space-based remote sensors because the lidar signal attenuates in the cloud layers' upper three optical depths.

The lidar on the CALIPSO satellite observes attenuated backscatter in 30 m vertical range bins from ~90 m footprints spaced every 300 m along the subsatellite track. The instrument records backscattered light in co- and cross-polarization channels at 532 nm and in the co-polarized channel at 1,064 nm. CALIPSO and CloudSat were launched together in April 2006, and they began returning data from within the A-Train satellite constellation by July 2006. From the beginning, operators navigated CloudSat to collect data from along the same ground track as CALIPSO and within a few tens of seconds spaced in time. The two active remote sensors' data are merged to form a geometric layer characterization product described by Mace and Zhang (2014). For the first year of data collection, CALIPSO pointed 0.3° from nadir but was pointed 3° forward of nadir in August 2007 to minimize specular reflection from horizontally oriented ice crystals. In the analysis that follows, we use all day and night data from all longitudes during calendar years 2007–2010 between 40°S Latitude and 75°S Latitude.

The phase identification algorithm applied to the CALIPSO data (Mace et al., 2020) builds on Hu et al. (2009). Hu et al. (2009) examined the layer-integrated co-polar and cross-polar layer-integrated attenuated backscattered laser power from layers that fully attenuate the lidar beam. Based on the early work of Platt (1977),

Hu et al. (2007) show that this method of phase identification requires that the layer is fully attenuating allowing for the transmissivity of the layer to be set to zero, thereby making the problem mathematically tractable. In Mace et al. (2020), we use physical reasoning derived from Mie theory to identify when measurements from a supercooled layer are inconsistent with an assumption of liquid-phase droplets. This reasoning is based on an understanding that there is a relationship between the lidar ratio and the effective radius. Hu et al. (2009) and references therein derive equations for the lidar ratio for fully attenuating liquid clouds, and in Mace et al. (2020) we use aircraft in situ data to derive a regression relationship between the lidar ratio and effective radius. We show that liquid-certain clouds (those that have temperatures greater than freezing) cluster within a predictable region of the layer integrated depolarization ratio-layer integrated attenuated backscatter space where the effective radius is greater than 0 and less than about 50 μm. We simply establish thresholds within this space that encompass this liquid cloud region. Supercooled cloud volumes that fall outside of the region enclosed by these new thresholds are assumed to have done so because of the presence of ice crystals that alter either the attenuated backscatter (i.e., plate-like crystals) or the volume-integrated depolarization ratio (nonspherical and non specularly reflecting crystals). Such volumes are defined as mixed phase due to the presence of ice crystals immersed in the supercooled liquid. We documented an error rate of less than 0.5% based on known liquid layers that return data in the phase diagram's mixed-phase region. Our methodology differs from that described by Hu et al. (2009), where they use conservative thresholds tuned to the presence of ice-dominant layers. We also demonstrate in Mace et al. (2020) and below through comparison to CloudSat radar reflectivity that layers that are defined to be mixed phase using this technique have radar reflectivities consistent with active precipitation processes.

3. Observing System Simulation Experiment (OSSE)

To demonstrate the challenge of diagnosing MPC when observing with depolarization lidar from above, we employ an OSSE based on model output from the Environment and Climate Change Canada (ECCC) Global Environment Multiscale numerical weather prediction model. The model output was created for the EarthCare project (Illingworth et al., 2015) and uses a 250 m horizontal and 100 m vertical grid spacing. The model was run using a double moment microphysics scheme (Milbrandt & Yau, 2005) and output was created for a transect that runs southwestward from near the southwest coast of Greenland to a point in the western Atlantic ~500 km northwest of Bermuda. INP simulated in the model was based on Meyers et al. (1992) that would predict ~10 INP L^{-1} at −10C. Secondary ice processes in the model included a simplified version of rime splintering (Hallet & Mossop, 1974). Cloud droplet number concentrations in the simulation were ~100 cm^{-3} and the typical number concentration of snow crystals was 5 L^{-1}. The transect was specifically designed to provide a simulation that had substantial mixed phase clouds. We focus on shallow clouds with tops below 4 km in this analysis that include ~3,000 vertical profiles.

The co- and cross-polar lidar attenuated backscatter from above and below was simulated using the methodology described in Cesana and Chepfer (2013). Lidar Attenuation due to Rayleigh scattering was simulated following Bucholtz (1995). Aerosol below cloud base was assumed to have an optical depth of 0.1 between the surface and the liquid cloud base following the SO results reported by Alexander and Protat (2019). The aerosol was assumed to be composed of dry sea salt and have a depolarization ratio of 0.03 and extinction to backscatter ratio of 25 following Haarig et al. (2017). All liquid-phase radiative properties are calculated using Mie Theory (Bohren & Huffman, 2009). The lidar ratio of ice crystals was assumed to be 35 (Josset et al., 2011) and have depolarization ratio of 0.3 (Sassen et al., 1992). W-Band Radar reflectivity was calculated using the approach in Posselt and Mace (2015: see Appendix B of that paper) using the backscatter cross section model of Hogan and Westbrook (2014). The mass and area dimensional relationships of rimed dendrites were assumed (Mitchell, 1996). Ice crystal fall speed was simulated using the methodology of Mitchell and Heymsfield (2005).

Figure 1 shows a representative precipitating mixed phase profile from the ECCC simulation and Table 1 lists the various properties of this profile and the simulation results. With a visible optical depth of ~15 and vertically integrated liquid water path (LWP) of 149 g m^{-2}, this profile is typical. Snow occurs from the upper most vertical level down to the surface although the water content and extinction of the snow are several orders smaller than that of the liquid. There is 7 g m^{-2} of total condensed ice in this column with a precipitation rate of 1.7 mm day^{-1} at cloud base just below 3 km where the radar reflectivity is −3.9 dBZe.
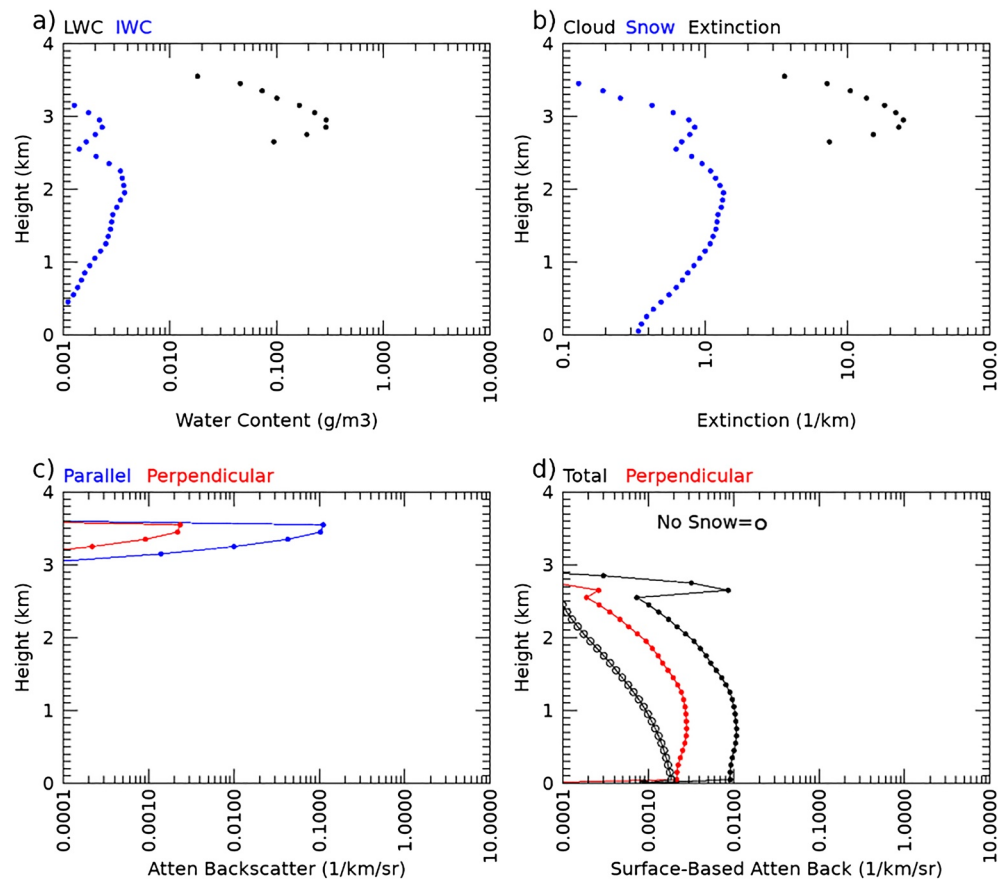
Figure 1. OSSE result for a profile from the ECCC EarthCare transect near 63.3°N and 54.8°W. (a) Water content of liquid and ice (blue). (b) Extinction due to liquid and ice (blue). (c) Lidar attenuated backscatter as observed from above for parallel (blue) and perpendicular (red) polarizations. (d) Lidar attenuated backscatter as observed from a surface-based lidar. Black open circles indicate aerosol and molecular scattering (i.e., no snow) while the red symbols indicate perpendicular and black parallel polarizations.

Simulated lidar observations from above are shown in Figure 1c. We find that the peak lidar attenuated backscatter of 0.1 km^{-1} sr^{-1} is at cloud top and the signal decays rapidly from cloud top due to extinction of the lidar beam by water droplets. The signal decreases by an order of magnitude in the first 500 m.

We test two methods for identifying phase from cloud top. In addition to the method described in Mace et al. (2020), we also simulate the phase diagnostic method in Cesana and Chepfer (2013). Both of these are based on depolarization ratio although the Cesana and Chepfer (2013) method examines the peak depolarization ratio in the first three optical depths. Both methods require the depolarization signal to exceed a threshold based on the magnitude of the attenuated backscatter. In Table 1, we list the results of the tests for the column in Figure 1. The maximum depolarization ratio in the top three optical depths does not exceed the Cesana and Chepfer (2013) threshold nor does the layer integrated depolarization ratio exceed the Mace et al. (2020) threshold. Thus both methods would not diagnose this profile as MPC. The reason for this incorrect diagnosis is as we hypothesized earlier. Even though snow is clearly present throughout the column, the backscatter due to the liquid phase dominates the total depolarization signal. The high values of attenuated backscatter in liquid clouds cause significant multiple scattering that results in increasing depolarization ratios even in the absence of ice. Because the depolarization ratio increases due to multiple scattering, the thresholds to identify ice in a high attenuated backscatter environment needs to be large. Typically, there is not enough ice present in a mixed phase cloud to exceed those thresholds.

From below, a lidar would have little trouble identifying this column as mixed phase. Figure 1d shows the simulated signal from below. The peak lidar attenuated backscatter occurs at cloud base and decays rapidly

Table 1
Physical and Observational Quantities of the ECCC Model Profile in Figure 1

Physical quantity	Values
Latitude and longitude	63.3°N and 54.8°W
Vertically integrated liquid water (LWP) g m^{-2}	149
Vertically integrated ice water (IWP) g m^{-2}	7.0
Liquid phase optical depth	14.5
Ice phase optical depth	2.8
Precipitation rate (mm day^{-1})	1.7
W-Band dBZe at cloud base	−3.9
Ice phase diagnostics	
Cesana and Chepfer (2013) depol threshold	0.0477
Maximum depol ratio in top three optical depths	0.02
Mace et al. (2020) integrated depol threshold	0.10
Observed integrated depol value	0.02
Total sub-Cloud attenuated backscatter (km^{-1} sr^{-1})	0.5
Sub-cloud attenuated backscatter (aerosol and molecular only) (km^{-1} sr^{-1})	0.09
Sub-cloud depolarization ratio	0.35
Sub-cloud depolarization ratio (aerosol only)	0.03

with height. Lidar return from the snow falling from the liquid layer rises above the background attenuated backscatter due to assumed sea salt aerosol and molecular scattering by approximately a factor of 5. The depolarization ratio of the snow also exceeds that due to sea salt by approximately a factor 10.

Figure 2 shows the results of examining all mixed phase profiles in the ECCC transect. From above, the Mace et al. (2020) method correctly identifies 3% of the mixed phase profiles while the Cesana and Chepfer (2013) method would correctly identify 8.6% as mixed phase. What we did not attempt to simulate here is the contribution from oriented ice crystals that would increase the total fraction of the Mace et al. (2020) diagnostic by ~30%. Cesana and Chepfer (2013) do not account for oriented ice crystals that typically have very low depolarization ratios because of specular reflection. Regardless of the details however, the methods using lidar from above would have a >90% error rate in this mixed phase environment. From below, we examine first our dBZe threshold of −20. This reflectivity is associated with a precipitation rate of 0.05 mm day^{-1}, a vertically integrated ice water path of 1 g m^{-2}, and is associated with a typical ice crystal number density of 10 m^{-3}. If we arbitrarily set a lidar detection threshold of a factor of 2 above the aerosol and molecular background (~3 dB), then of those profiles with a sub-cloud radar reflectivity of −20 dBZe or greater, we would detect 83.5% of them with the surface-based lidar method. The depolarization ratio is in excess of five times the aerosol background in 92% of profiles. Of the profiles that have >1 g m^{-2} of ice, 81% of them have a sub-cloud dBZe in excess of −20. Thus the OSSE results using the ECCC model output are strongly supportive of the hypothesis that mixed phase clouds are severely undercounted when viewing by lidar from above. While the surface-based result may also undercount, the undercount percentage is likely less than ~15% of the total mixed phase columns.

4. Observational Analysis

Our objective in this study is to explore the occurrence of SO marine boundary layer (MBL) clouds that are mixed phase. Therefore, we selectively sample satellite and surface-based data to isolate those layers. We require layers defined by the merged CloudSat and Calipso data to have bases below 2 km and layer tops with temperatures greater than −40°C and less than 0°C. For the surface-based data, we require cloud bases to have temperatures less than 0°C and exist below 2 km. For reasons that will become evident, we separate
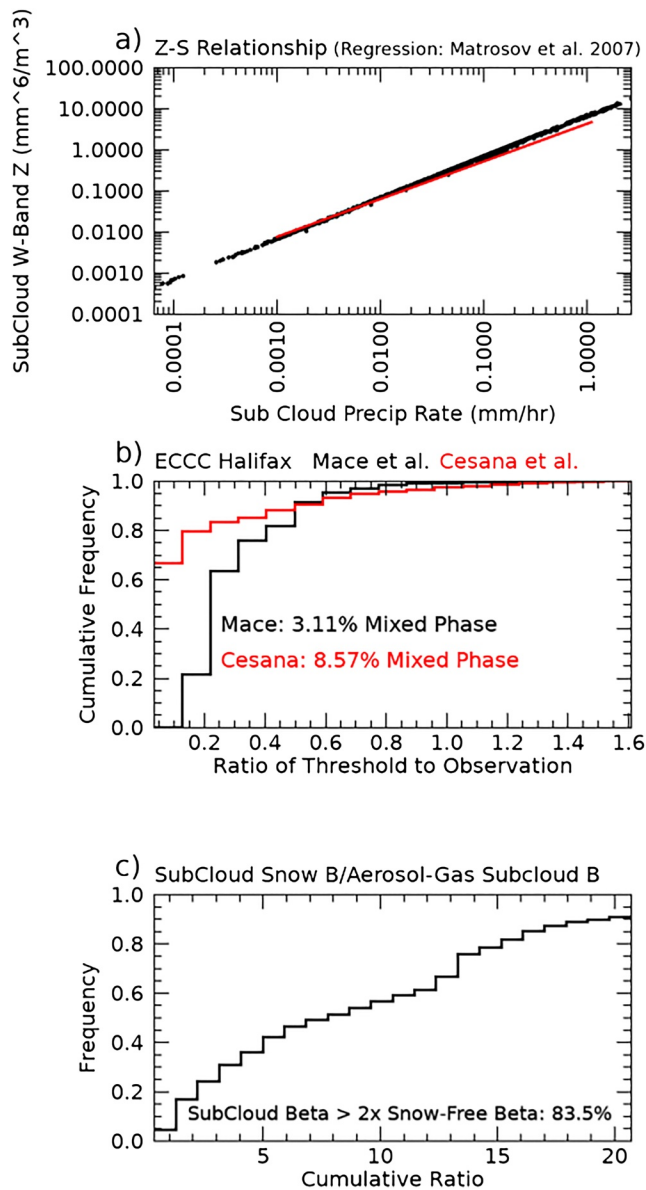
Figure 2. Statistical results from the OSSE shallow clouds (tops < 4 km) that were composed of liquid cloud and solid precipitation. (a) A scatter plot of sub-cloud W-Band dBZe as a function of sub-cloud precipitation rate (black dots). The red line shows a regression relationship derived from measurements in Matrosov et al. (2007) that demonstrates that modeled snowfall is consistent between precipitation rate and radar reflectivity. (b) Shows the cumulative distribution of the ratio of the diagnosed depolarization quantity from the mixed phase cloud compared to a threshold value from the Mace et al. (2020) and Cesana and Chepfer (2013) diagnostics. Any number of this ratio less than 1 indicates that the layer would not have been considered mixed phase. The inset shows the fraction of cases correctly diagnosed as mixed phase. (c) The ratio of the subcloud total attenuated backscatter to the snow-free attenuated backscatter. Any number >1 indicates that the attenuated backscatter that includes snow is greater than the aerosol and molecular signal. The inset shows the fraction of cases where this ratio is >2—an arbitrary indicator that the layer would be correctly diagnosed as mixed phase.

layers by geometric thicknesses of less than 1, 1–3, and 3–5 km. Within each of these thickness categories, we further separate the layers by those precipitating from those not precipitating. Following Liu et al. (2008), we define precipitation as a column-coincident radar reflectivity factor above −20 dBZe.

Layer thickness is estimated by combining the lidar data with measurements from coincident millimeter radars. A limitation is that CloudSat is unable to observe below 1 km (Marchand et al., 2008). From above, any layer with lidar-observed tops that are below 1 km are, by definition, placed in the 1 km thickness bin. The thickness of layers with tops in excess of 1 km observed by CALIPSO are determined from the combined CloudSat and CALIPSO cloud mask (Mace & Zhang, 2014). From below, thickness is assigned based on coincident millimeter radar data. In cases where the layer is below the detection threshold of the radar, we assign the layer to the 1 km thickness class with reasoning based on the Cloud-Sat-CALIPSO combined data that non precipitating layers that are not sensed by the surface-based radar would tend to have thicknesses less than 1 km since precipitating layers would not be below the detection threshold of the surface-based radars.

4.1. Occurrence

Aside from two significant outages in February–March 2009 and in January 2010, we analyze approximately two million merged CALIPSO and CloudSat profiles per month between 40°S Latitude and 75°S Latitude. Approximately 86% of the columns contain a hydrometeor layer. Approximately ½ of the cloudy columns were composed of a single hydrometeor layer, while ∼½ of those were composed of clouds based in the MBL. Of the boundary layer clouds, a bit more than half of them were fully attenuating and were, therefore, candidates for the phase estimation algorithm amounting to ∼16.5 M observations over the 48 months. The MBL clouds that were not fully attenuating typically had geometric thicknesses less than 1 km. Of the fully attenuating MBL clouds, ∼51% were precipitating (Table 2). Precipitation occurs predominantly in clouds that have a geometric thickness >1 km.

The latitudinal distribution of the ship-based remote sensing data (hereafter surface data) are summarized in Figure 3. The latitudinal distribution of the measurements is uneven. The maximum in the most southerly latitude bin is because the R/V Aurora Australis spent considerable time at and in transit between the Mawson, Davis, and Casey Antarctic Stations during the summer resupply activities during the MARCUS campaign, and CAPRICORN I data all occur north of 55°S. The high overall coverage of clouds in the SO and the predominance of low-level clouds is evident. Geometrically thin layers (<1 km thickness) compose the largest fraction of low-level supercooled clouds in the surface data (Table 3). Differences between the surface and satellite data appear in the fraction of geometrically thin low-level clouds. This difference can be understood by differences in sampling. The satellite data are averaged to 2 km footprints because of the need to combine with CloudSat whereas the surface data sample much smaller regions typically being composed of averages compiled over several tens of seconds. In averaging the satellite data, it is much more likely that the highly reflective surface is sampled. If we

Table 2
Relative Occurrence Statistics of Fully Attenuating Oceanic Columns Observed by CALIPSO Between 40° and 75°S From January 2007 Through December 2010 Segregated by Layer Thickness and Presence of Precipitation

Occurrence statistics of space-based fully attenuating lidar layers based in the MBL with layer top temperatures <0°C

Layer thickness	Layers fully attenuating (fraction of total fully attenuating layers—bottom cell)	Precipitating layers (fraction of total layers in thickness range)	MPC (fraction of precipitating layers in thickness range)
0–1 km	0.39	0.14	0.0
1–3 km	0.49	0.71	0.03
3–5 km	0.11	0.97	0.09
Total	16,485,317	0.51	0.04

Note. The normalization factor is listed in the Parentheses of each column. The total number of fully attenuating layers that are included in the analysis is shown in the bottom cell of column 2. The fractions in the layer thickness rows and column 2 add to 1. The total number of fully attenuating profiles in each thickness category can be calculated by multiplying the fraction in column 2 by the number in the bottom cell of column 2. The fractions in columns 3 and 4 are relative to the number of fully attenuating columns in that thickness category.

remove the requirement that the layers are fully attenuating, both data sets agree that ~80% of the cloud occurrence is due to layers less than 1 km thickness based in the MBL. Both data sets also agree that these geometrically thin layers rarely precipitate (18% surface and 14% space), but the precipitation is mostly supercooled liquid when they do.
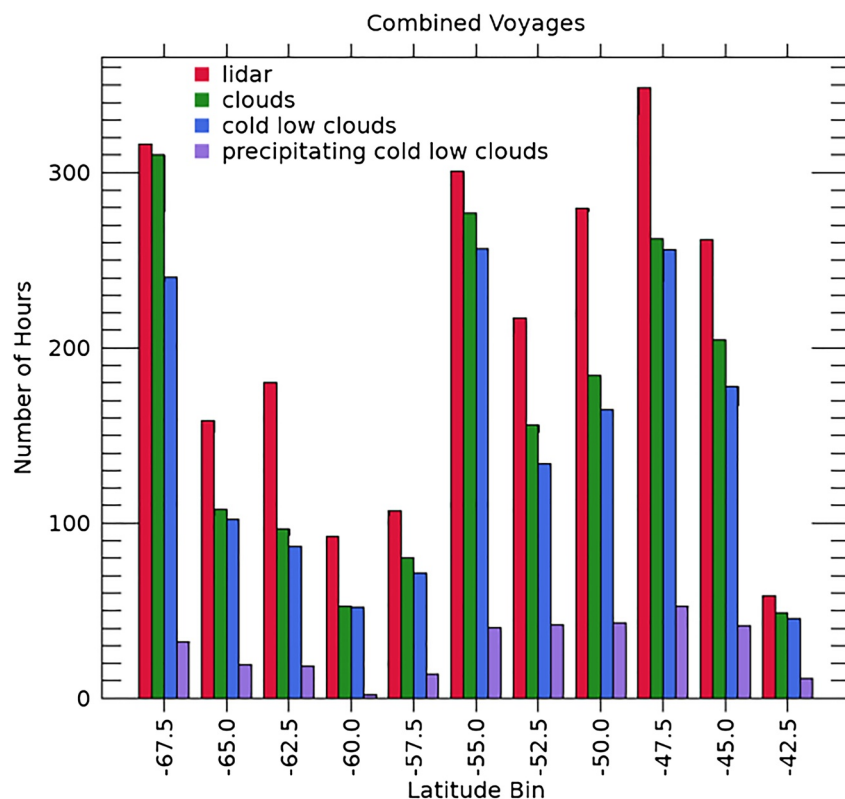

Figure 3. The latitudinal distribution of surface based data showing the number of hours of measurements as described in the legend. The red bars show the total number of hours surface-based lidar data are available in that latitude bin. Green shows the number of hours with an identifiable cloud base. Cold clouds are those with a layer top temperature less than freezing where the top is from coincident W-Band radar. Precipitating layers are those with W-Band radar reflectivity greater than −20 dBZ below the lidar cloud base.

Table 3

As in Table 1 Except for Layers Observed From Surface Lidars During the CAPRICORN I, CAPRICORN II, and MARCUS Voyages

Occurrence statistics of surface-based lidar layers based in the MBL with layer top temperatures <0°C. All layers seen by radar (attenuating)

Layer thickness	Layers fully attenuating (fraction of total fully attenuating layers)	Precipitating layers (fraction of total layers in thickness range)	MPC (fraction of precipitating layers in thickness range)
0–1 km	0.64	0.18	0.30
1–3 km	0.25	0.58	0.62
3–5 km	0.11	0.66	0.82
Total	55,119	0.33	0.55

However, examining the partitioning of phase in the geometrically thin layers, we find a substantial difference between the surface and satellite data. The surface data indicate that 30% of the precipitation from the geometrically thin layers is ice. In contrast, the satellite data essentially diagnose no ice phase to three decimal points in the geometrically thin and fully attenuating precipitating clouds. This difference extends to the deeper layers, with just 3% and 9% of the precipitating layers in the 1–3 and 3–5 km thickness bins identified as containing ice (in reasonable agreement with the OSSE results). In contrast, the surface data find that 62% and 82% of these columns have ice phase precipitation, respectively. The cause and implications of this difference in MPC occurrence between satellite and surface is the primary focus of this study.

Figure 4 expands the summary results in Tables 2 and 3 in terms of the liquid frequency as a function of the layer top temperature. The dominant geometrically thin layer types agree reasonably well between the two data sets. Precipitation remains rare in the geometrically thin layers
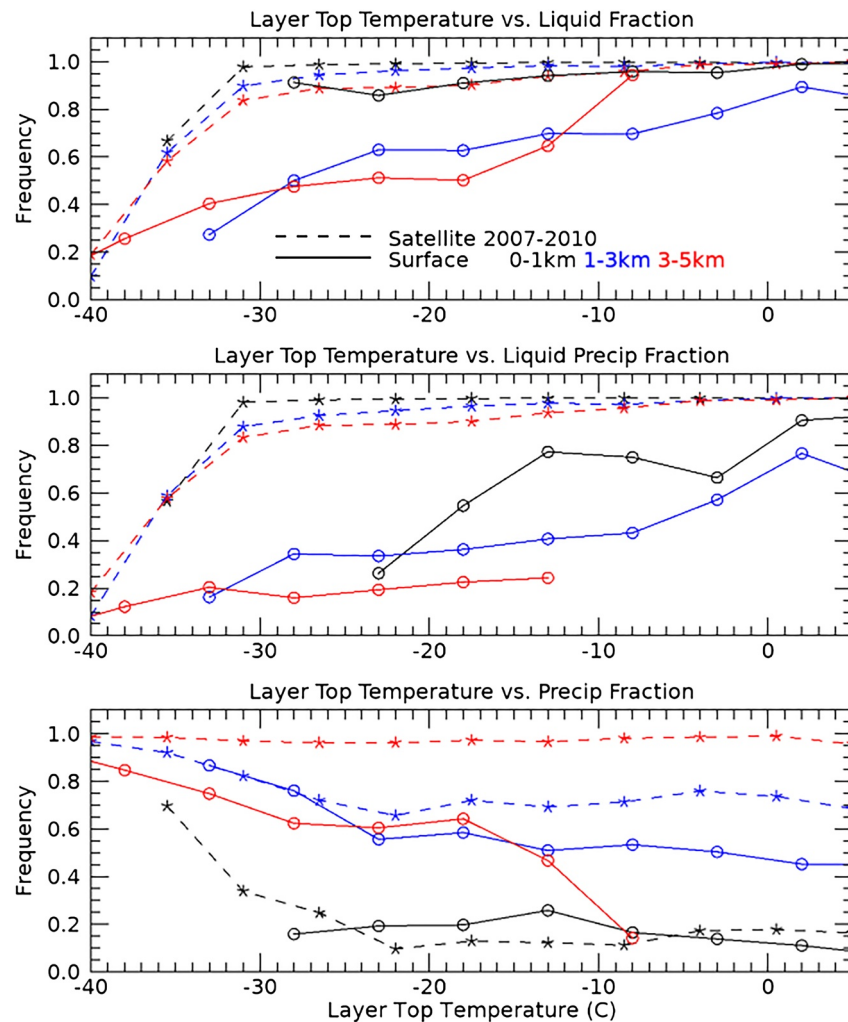

Figure 4. Frequency of occurrence as a function of layer top temperature of: (top) mixed-phase clouds layers for different layer thicknesses as described in the inset, (middle) fraction of time precipitation is diagnosed to be liquid when precipitation is observed, and (bottom) the frequency of precipitation. Dashed curves are for satellite observations (CALIPSO and CloudSat) and solid curves represent data collected from ship-base lidars and W-Band radars.

in both data sets to temperatures approaching −30°C. In the thicker layers, precipitation occurrence increases monotonically as the layer top temperature decreases in both data sets. However, for thicker layers, the phase differences between the two data sets amplify as the layer top temperature decreases, especially for precipitating layers. Somewhat independent of layer thickness, we find that the frequency of MPC in the surface data decreases monotonically from near 1 for the layers near the freezing point to near 0 as the layer top temperature approaches −40°C. On the other hand, MPC remains rare in the satellite data for all temperatures down to layer top temperatures approaching −30°C. For temperatures lower than approximately −30°C, the frequency of liquid begins to decrease substantially in the satellite data as the layer tops cool to near the homogeneous freezing point of water.

The discrepancies between surface-based and space-based MPC occurrence frequencies in the precipitating profiles suggest that CALIPSO cannot sense the presence of some large fraction of MPC clouds. Two possible reason may cause this discrepancy. First, the ice hydrometeors not sensed by the space-based lidar may exist at altitudes below which the lidar fully attenuates (typically taken to be optical depth three from the top). Another possibility is that the ice crystals are present in concentrations that are too low to be discriminated from the liquid droplets that dominate the light scattering near the cloud top. The OSSE results indicate that the latter reason is the primary cause of the discrepancy, although it is possible that the simulation is not a completely accurate representation of nature. Regardless of the reasons, the data suggest that space-based lidar severely undercounts the occurrence frequency of MPC in the supercooled MBL clouds. We next examine the geographic distribution of CALIPSO-observed MPC to shed light on the source of the differences between the surface and satellite data sets.

4.2. Geographic Distribution of Mixed Phase Clouds

One of the intriguing results in Mace et al. (2020) was a significant latitudinal gradient in MPC over the SO in the CALIPSO data. The ice phase in supercooled liquid clouds near Antarctica was observed to occur much less frequently than in supercooled clouds over warmer waters farther north. In Figure 5, we present a map of MPC occurrence for the 1–3 km thickness clouds with cloud top temperatures between −20 and 0°C. We choose the 1–3 km thickness range because these clouds precipitate often enough to develop useful statistics on MPC occurrence. The temperature range bounds a region where ice nucleating aerosols become increasingly active (McCluskey et al., 2018) while remaining well removed from the homogeneous freezing point. We show the 95% confidence interval distribution (Lancaster, 1961) as a histogram and place contours of this confidence's 25% value on the map. Confidence intervals decrease poleward and equatorward of these contours. We do not plot pixels with 95% confidence that exceeds 50% of the occurrence frequency. Low values of confidence are due to smaller numbers of this cloud class's occurrences in the latitude and longitude bins. Also plotted in Figure 5 as a red dashed contour is the oceanic Antarctic Polar Front (APF), as reported in Freeman and Lovenduski (2016).

We find that MPC occurrence from CALIPSO in the precipitating 1–3 km clouds has a significant latitudinal gradient increasing in occurrence from just a few percent near the Antarctic continent to values approaching 10% from 45°S and northward. The meridional gradient in MPC is not uniform but demonstrates a weak gradient from the Antarctic coast to about 55°S and then increases much more rapidly northward. The data also suggest a longitudinal asymmetry in the location of the latitudinal gradient. For instance, the maximum gradient magnitude seems to occur closer to 45°S in the Atlantic and Indian sectors. In contrast, the gradient tends to be weaker and displaced to near 55°S in the SO's Pacific sector. The latitudinal gradients are also evident in clouds with tops that have temperatures less than −20°C. However, the gradients near the APF are weaker in magnitude.

We note that the longitudinal asymmetry in MPC occurrence closely follows the location of the APF. The APF is just one of several distinct oceanographic fronts that characterize the eastward flowing Antarctic Circumpolar Current (Sokolov & Rintoul, 2009). The APF has the most distinct surface thermal contrast of these frontal boundaries (Freeman & Lovenduski, 2016). We note from Figure 5 that the APF has similar longitudinal asymmetries with, for instance, a bulge to lower latitudes in the Atlantic and the Indian Ocean and a displacement to higher latitudes in the Pacific. While we do not plot it here, inspection of Figure 4 in Freeman and Lovenduski (2016) shows that the SST gradient's magnitude is strongest in the Atlantic and
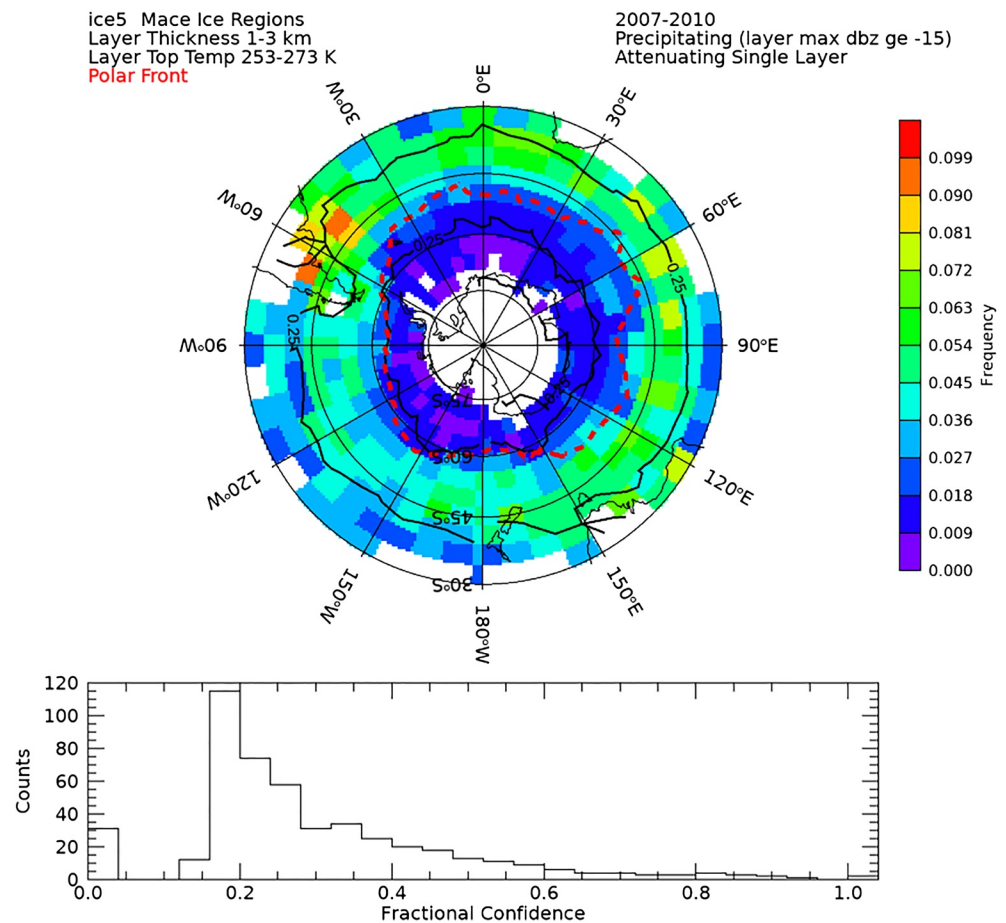
Figure 5. The occurrence frequency of mixed phase cloud from CALIPSO for MBL clouds of 1–3 km depth with top temperatures between −40 and 0°C. The frequencies are relative to the occurrence of this class of clouds in the CALIPSO-CloudSat data set for the period analyzed. The red curve shows the annually average location of the Antarctic Polar Front (APF), as reported in Freeman and Lovenduski (2016). The black contours show where the confidence interval in the frequencies of occurrence are 25% of the value. The 95% confidence intervals as a fraction of the observed values are shown in the bottom frequency distribution.

Indian sectors exceeding 2 K/100 km. Freeman et al. (2016) show that during the period between 2002 and 2014 the zonal mean spatial variability in the APF was less than 0.5° of latitude.

In contrast, the SST gradient is weaker and less pronounced where it is displaced further south in the Pacific. As shown in J. Liu et al. (2011), the APF thermal gradient's variable magnitudes are associated with variations in sensible heat fluxes from the ocean to the atmosphere. The fluxes are significantly larger in the Atlantic and Indian ocean compared to the Pacific with a geographic pattern similar to that of the MPC gradients in Figure 5. The CALIPSO and CloudSat data's poor sampling statistics make a quantitative evaluation of this apparent association between the gradient magnitudes challenging to evaluate quantitatively. We do find, however, that the correlation between the latitude of the maximum gradient in MPC and the latitude of the APF as a function of longitude is 0.86 and that the gradient values at the latitudinal maximum are more than a factor of 2 larger than the gradient values to the north and to the south. The latitudinal dependence in the zonal mean is further illustrated in Figure 6, where we plot the zonally averaged liquid frequency as a function of cloud top temperature like in Figure 4. The difference between the Northerly and Southerly latitudes is evident. By separating the surface data at the approximate Latitude (50°S) of the APF near the mean longitude of the MARCUS and CAPRICORN campaigns (~140°E) we find that the surface data also show that MPC is more frequent north of the APF for a given cloud top temperature. So, the gradient implied in Figure 4 is, we conclude, a physical feature (discussed in more detail in Section 5), that is
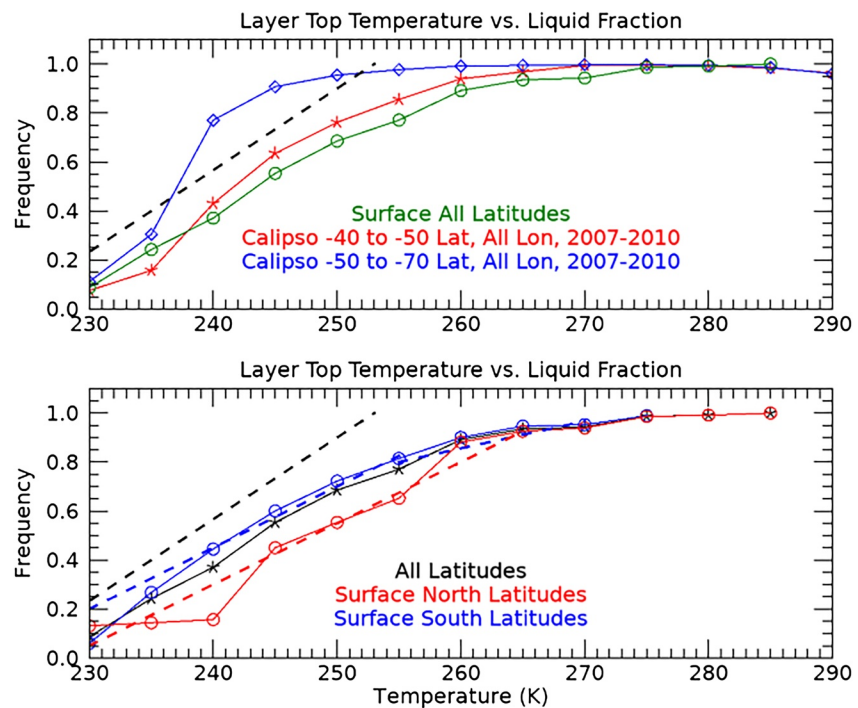
Figure 6. As in the top panel of Figure 2 except we separate the CALIPSO data (top) and surface data (bottom) by latitude. Also shown (black dashed line) is the phase parameterization introduced by Kay et al. (2016). The red and blue dashed lines in the bottom panel show $1 - f$ of the parameterizations of the phase occurrence derived from the ship-based data described by Equation 1 and Table 3.

directly associated with the APF. However, the magnitude of MPC's occurrence when viewed from above is much lower than what is observed in surface-based data.

To understand the discrepancy in MPC occurrence between the surface and satellite observations the OSSE notwithstanding, let us summarize the evidence presented thus far. First, overall INP abundance in the SO is very low. McCluskey et al. (2018) suggest that at $-10°C$ INP concentrations are on the order of 1 m^{-3}. Second, we find the latitudinal gradient in MPC in both data sets, suggesting that it is a real feature. Third, we have identified an association between the MPC gradient and the APF thermal boundary. Along and north of the APF, the thermal contrast would induce more vigorous convective motions driven by heat and moisture fluxes as cold air masses behind cold fronts pass equatorward of this thermal boundary. These convective motions can loft ice crystals to cloud top. However, they would also produce ice via secondary ice processes so that the concentration of ice crystals in the enhanced convective motions is not limited by the low INP abundance.

Secondary ice production (SIP) is a broad term used to describe a family of microphysical processes that convert water droplets into ice crystals independent of the ice phase's direct or primary nucleation onto INP. See Korolev and Leisner (2020) and Field et al. (2017) for recent reviews of SIP. Our contention that SIP is more active along and north of the APF is consistent with our understanding of SIP in shallow cumuli. Mossop et al.'s (1970) early paper was based on airborne data collected in winter supercooled boundary layer clouds near Tasmania's western coast. Mossop's early results were largely replicated and amplified by Huang et al. (2017, 2021). They found that while INP concentrations were a predictor of the occurrence of the ice phase, data from cumulus penetrations showed ice particle concentrations that were a factor of 10^4 greater than the measured INP concentrations. Earlier reviews of the topic (Mossop, 1986; Prup-pacher & Klett, 1997), as well as Korolev and Leisner (2020), identify the primary SIP mechanisms in su-percooled clouds. These include mechanical fracturing of fragile crystals (e.g., Griggs & Choularton, 1986; Vardiman, 1978), freezing and subsequent fracturing of drizzle-sized liquid droplets (e.g., Koenig, 1963; Ono, 1972), and rime splintering (Hallet & Mossop, 1974; Lasher-Trapp et al., 2016). Recently, Keinert
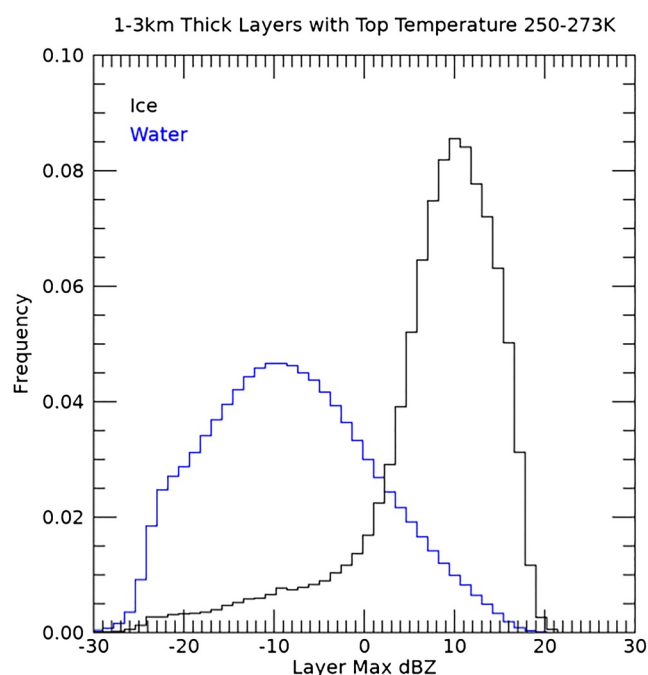
Figure 7. Distributions of layer maximum dBZ from CloudSat in 1–3 km thick clouds between −20 and 0°C for all layers (black) and layers where CALIPSO observes mixed phase conditions.

et al. (2020) found an enhancement in droplet shattering probability for drizzle droplets composed of a dilute sea salt solution falling at terminal velocity. A rich and growing body of observational (e.g., Korolev & Leisner, 2020; Lauber et al., 2018; Lawson et al., 2015) and theoretical (e.g., Sullivan et al., 2017, 2018) literature exists on this topic. The processes identified are likely all active under the conditions appropriate to their unique physics that require precipitation hydrometeors to be lofted to temperatures between roughly −5 and −15°C.

The creation and lofting of drizzle-sized droplets and large ice crystals require updrafts of sufficient strength. The terminal velocity of droplets between 300 μm and 1 mm ranges from ~1.2 to 4 m s^{-1} at sea level (Gunn & Kinzer, 1949). For ice crystals to be sensed by the CALIPSO lidar, either the updrafts must also have lofted the ice particles to near the tops of the predominantly liquid clouds or the ice crystals were nucleated near cloud top by either primary or secondary processes. While we have no direct measure of updraft speed from the A-Train, we can test the hypothesis that precipitation sized hydrometeors are present when MPC is diagnosed with CALIPSO. We do this by examining coincident radar reflectivity from CloudSat. Figure 7 shows that the predominant liquid water layers tend to have maximum reflectivities that distribute broadly near −10 dBZ. The profiles that populate the blue histogram that are diagnosed by CALIPSO to be liquid water include nonprecipitating and precipitating columns. We contend, based on analysis of the surface-based data, that the precipitation could be either ice phase or liquid but we do not attempt to objectively distinguish the phase of the precipitation from the CALIPSO-CloudSat data when the precipitation occurs beyond the point in the vertical profile where CALIPSO attenuates. In comparison, layers that have been diagnosed by CALIPSO to be MPC have much higher radar reflectivities that have a narrow peak near +10 dBZ with nearly all observations above 0 dBZ. There is little doubt that nearly all layers diagnosed by CALIPSO to be MPC do indeed contain precipitation-sized hydrometeors—almost certainly snow.

5. Discussion

In the absence of updrafts of sufficient strength to induce SIP for clouds that are much warmer than the homogeneous freezing temperature of the water, we question whether the observed concentrations of INP in the SO are sufficient to explain the remote sensing measurements. Revisiting the OSSE, we recall that the downward looking lidar methods incorrectly diagnosed the presence of ice in the mixed phase layers >90% of the time even though these layers were lightly precipitating snow. The number concentration of snow in these clouds averaged ~5 L^{-1} with a standard deviation of approximately a factor of 2. We also calculated by what factor the number concentration of snow particles would need to increase before the Mace et al. (2020) method would diagnose a layer-integrated depolarization ratio sufficient to correctly diagnose the layers as mixed phase. We arrived at a mean factor of 1.8 with a median of 2.5. This implies that, on average, about a factor of 2 more ice crystals would result in a correct diagnosis of phase much more often in the OSSE. Recall, however, that the INP assumed in the ECCC model run was based on the Meyers et al. (1992) scheme that would put about 10 L^{-1} of INP at temperatures of −10C. This number of INP is reasonably consistent with the number concentration of snow particles that we calculated of ~5 L^{-1}. However, the number of INP in the SO has recently been measured and found to be much smaller than predicted by Meyers et al. (1992). McCluskey et al. (2018) finds INP on the order of 1 m^{-3} (0.001 L^{-1}) based on data collected during the CAPRICORN I voyage in 2016. Results presented in McFarquhar et al. (2021) from the 2018 voyages confirm values of INP in this range. Thus, it appears that while the OSSE results demonstrate the challenges, it is likely that the actual number of ice crystals from primary nucleation is much smaller in the SO than what is simulated in the OSSE.

Table 4
Values for the Parameterization of Ice Occurrence Fraction, f, of the Blue and Red Dashed Lines in Figure 4

Region	T_{ice} (K)	M (K^{-1})	T_{cold} (K)	f_{warm}	f_{cold}
North warm (NW)	273	90	262	0	N/A
North cold (NC)	262	40	238	$f_{nw}(T = T_{cold})$	1
South (S)	268	40	238	0	1

Note. The latitudinal boundary between north and south is taken to be 52°S.

Therefore, it seems reasonable that several orders of magnitude more ice crystals per unit volume are required than could theoretically be nucleated from primary INP for the downward looking lidars to identify MPC. These calculations help us understand the discrepancy between the surface and satellite data. Much lower ice concentrations can be detected from below the cloud, where the hydrometeors have grown to precipitation sizes in their descent through the cloud layer and are not masked by liquid droplets. It remains for future work to quantify the concentration of ice crystals below MPCs from observations in the SO.

In Figure 6, we plot the parameterization used by Kay et al. (2016) and Frey and Kay (2018). This parameterization is also denoted as CLDMOD in Schneider et al. (2020). That parameterization reasonably represents the occurrence of CALIPSO-derived MPC south of the APF. However, the parameterization produces too little MPC north of the APF. A careful examination of Frey and Kay (2018, their Figure 1) shows that their modified parametrization reduces the positive absorbed shortwave bias poleward of 50°S but the bias become negative (i.e., too much cloud cover) north of 50°S. Similar results can be seen in Varma et al. (2020). We offer the possibility that this response in absorbed shortwave bias is due to more ice and lower cloud cover occurring in the real atmosphere north of the APF than predicted by the CLDMOD parameterization that is based on the CALIPSO phase data.

When accounting for the occurrence of MPC from the surface data, it seems clear that the shallow convective detrainment parameterization used in earlier work and plotted in Figure 6 as the dashed black line does not represent the surface observations very well. We offer a set of alternative parameterizations that best represent the surface data with values listed in Table 4:

$$
\begin{aligned}
f_{region} &= f_{warm}; \text{for } T > T_{ice} \\
f_{region} &= \frac{(T_{ice} - T)}{M}; \text{for } T_{cold} < T < T_{ice} \\
f_{region} &= f_{cold}; \text{for } T < T_{cold}
\end{aligned}
\tag{1}
$$

In Equation 1, f_{region} is the occurrence frequency of MPC where region denotes north and south of 50°S (Table 3). f_{warm} is the frequency of MPC at the warm temperature limit of the line, T_{cold} and T_{ice} are the temperatures at the cold and warm extremes of the parameterized line, and M is the slope of the parameterized line. We plot $1-f_{region}$ in Figure 6. In the northern region, we suggest two lines valid at different temperatures to best represent the data.

If implemented in a model, these new parameterizations would result in decreased cloud cover. The decreased cloud cover would certainly cause a relapse of the surface SW radiation bias at the surface that Kay et al. (2016) attempted to fix via their modified parameterization, CLDMOD. We offer a potential solution. As discussed in Frey and Kay (2018), the primary sink of cloud water detrained from shallow convection is from the conversion of the detrained cloud water to precipitation. Figure 4 shows that the predominant geometrically thin cloud type rarely precipitates down to temperatures as low −30°C. The rarity of precipitation in the geometrically thin layers suggests that loss of condensate to precipitation is not rapid in these clouds. Therefore, these thin layers would be likely to persist in a model and reflect sunlight for a longer time if the sink of cloud water to precipitation were reduced. Modifying the loss rate of these shallow clouds to precipitation to better match observations has the potential to counter the effect of a more realistic phase parameterization (Equation 1). Experimentation is needed to confirm these speculations. However, as noted in Kay et al. (2016), the simple change that they made to the shallow convective detrainment was meant only to test the sensitivity of the atmosphere to phase, and the goal was to eventually constrain the model based on physical principles. We offer an incremental step in that direction with these results.

6. Conclusions

A clearer picture of the occurrence of snow in SO low-level clouds has emerged from this study. Geometrically thin (<1 km) supercooled clouds are rarely mixed-phase, and they dominate the overall coverage of supercooled low cloud layers. Geometrically thicker cloud layers precipitate more often, and that frequency increases with decreasing cloud top temperature. From the surface data sets, we find that ∼1/3 of precipitating geometrically thicker layers produce supercooled liquid precipitation in the SO data sets. Supercooled liquid drizzle would occur in situations where INP are not active at the cloud temperatures or where updrafts are too weak to loft precipitation to temperatures where secondary ice processes can initiate the ice phase. See Silber et al. (2019) for a recent and compelling example of supercooled liquid precipitation at McMurdo Station. However, we find a sharp discrepancy between the satellite and surface data in ice phase precipitation frequency. Of the layers that are thicker than 1 km and precipitating, we find that 62% (1–3 km) and 82% (3–5 km) produce ice phase precipitation when viewed from below by lidar, whereas only 3% and 9% show evidence of being MPC when viewed from above by lidar.

We conclude based on observations that are supported by an OSSE that the rarity and geographic pattern of MPC are due to the limitations of remote sensing MPC layers by nadir-observing lidar. Even in situations where primary INP produces ice, such ice would occur at concentrations that are too low for CALIPSO to distinguish from the background liquid drops. We contend that the geographic distribution of MPC that we do observe from CALIPSO (Figure 5) is due to the pattern of occurrence of secondary ice processes that become more active in more vigorous convective motions over warmer waters north of the APF. This is supported by the tendency of these MPC columns to have radar reflectivities consistent with the presence of large hydrometeors within what is likely relatively strong convective updrafts. Recent in situ observations of open cellular cumulus near Tasmania provide additional evidence for the dominance of secondary ice processes in shallow convection (Huang et al., 2017, 2021). It seems that secondary ice processes that would produce ice in high enough concentrations are less active over the relatively colder waters south of the APF, causing MPC to be observed less often by CALIPSO. Based on the measurement statistics from surface-based lidar, low number concentration ice precipitation from either primary nucleation mechanisms or weaker secondary processes produces ice precipitation in the more southerly latitudes much more frequently than observed by CALIPSO. However, the ice concentrations near cloud top are often below the detection threshold of CALIPSO.

These results call into question the phase parameterizations derived for supercooled liquid developed from CALIPSO data. While several studies show that these parameterizations significantly reduce the surface-absorbed shortwave bias in models, we contend that this improvement is for reasons that are not entirely consistent with observations. As evidence for this contention, we observe that while the surface-absorbed shortwave bias is improved south of the APF in models that use the modified parameterization, the bias tends to become negative north of the APF. This result is consistent with more MPC equatorward of the APF than poleward (Figures 5 and 6). We present an alternate parameterization of MPC that is consistent with the surface observations. Since this new parameterization is sure to cause the surface-absorbed shortwave bias to reoccur, we offer the possibility based on observations (Figure 4), that the predominant thin clouds only rarely precipitate. Therefore, these cloud layers possibley persist for a longer time than the present parameterizations allow for. Adjusting the liquid water sink processes in the geometrically thin layers to better match observations may be a step toward a more physically based solution.

A more detailed understanding of the aerosol-cloud-precipitation physics in the remote SO is needed. The importance of this region to the global climate is becoming increasingly evident. There are many reasons to expect that this region is unique on Earth due to the underlying oceanic processes, associated biology, and distance from anthropogenic aerosol sources. The SO is also undergoing broad changes due to a warming climate, recovering ozone, and other forcing factors. A more complete understanding of the role of primary and secondary ice processes that create precipitation in the ubiquitous boundary layer clouds that control the albedo and surface energy balance is needed, along with a better understanding of the biogeochemical cycles that modulate INP concentrations in the SO. The surface-based data collected between 2016 and 2018 allow us to gain some of that understanding, but the data are sparse in terms of longitude and season. A concerted observational strategy is needed to extend knowledge to the point where we can make definitive statements about the physical processes that control this region's cloud properties.

Data Availability Statement

All data used in this study are available in public archives. MARCUS data are available from the DOE ARM archive at https://adc.arm.gov/armlogin/login.jsp, SOCRATES data are available at https://data.eol.ucar.edu/project/SOCRATES, and CAPRICORN I and II data are available at https://doi.org/10.25919/5f688fcc97166.

References

Alexander, S. P., & Protat, A. (2019). Vertical profiling of aerosols with a combined Raman-elastic backscatter lidar in the remote Southern Ocean marine boundary layer (43–66°S, 132–150°E). *Journal of Geophysical Research: Atmospheres*, *124*, 12107–12125. https://doi.org/10.1029/2019JD030628

Bergeron, T. (1935). *On the physics of cloud and precipitation*. Procès Verbaux de la Séance de VU, GGI à Lisbonne 19S3.

Bodas-Salcedo, A., Hill, P., Furtado, K., Williams, K., Field, P., Manners, J., et al. (2016). Large contribution of supercooled liquid clouds to the solar radiation budget of the Southern Ocean. *Journal of Climate*, *29*, 4213–4228. https://doi.org/10.1175/jcli-d-15-0564.1

Bodas-Salcedo, A., Mulcahy, J. P., Andrews, T., Williams, K. D., Ringer, M. A., Field, P. R., & Elsaesser, G. S. (2019). Strong dependence of atmospheric feedbacks on mixed-phase microphysics and aerosol-cloud interactions in HadGEM3. *Journal of Advances in Modeling Earth Systems*, *11*, 1735–1758. https://doi.org/10.1029/2019MS001688

Bohren, C. F., & Huffman, D. R. (2009). *Absorption and scattering of light by small particles*. Wiley-VCH.

Bucholtz, A. (1995). Rayleigh-scattering calculations for the terrestrial atmosphere. *Applied Optics*, *34*(15), 2765–2773. https://doi.org/10.1364/ao.34.002765

Cai, W., van Rensch, P., Borlace, S., & Cowan, T. (2011). Does the Southern Annular Mode contribute to the persistence of the multidecade-long drought over southwest Western Australia? *Geophysical Research Letters*, *38*, L14712. https://doi.org/10.1029/2011GL047943

Ceppi, P., & Hartmann, D. L. (2015). Connections between clouds, radiation, and midlatitude dynamics: A review. *Current Climate Change Reports*, *1*, 94–102. https://doi.org/10.1007/s40641-015-0010-x

Cesana, G., & Chepfer, H. (2013). Evaluation of the cloud thermodynamic phase in a climate model using CALIPSO-GOCCP. *Journal of Geophysical Research: Atmospheres*, *118*, 7922–7937. https://doi.org/10.1002/jgrd.50376

Field, P. R., Lawson, R. P., Brown, P. R. A., Lloyd, G., Westbrook, C., Moisseev, D., et al. (2017). Secondary ice production – Current state of the science and recommendations for the future. *Meteorological Monographs*, *58*, 71–720. https://doi.org/10.1175/AMSMONOGRAPHS-D-16-0014.1

Findeisen, W. (1938). Kolloid-meteorologische Vorgänge bei Neiderschlags-bildung. *Meteorologische Zeitschrift*, *55*, 121–133.

Fossum, K. N., Ovadnevaite, J., Ceburnis, D., Dall'Osto, M., Marullo, S., Bellaicco, M., et al. (2018). Summertime primary and secondary contributions to Southern Ocean Cloud condensation nuclei. *Scientific Reports*, *8*, 13844. https://doi.org/10.1038/s41598-018-32047-4

Freeman, N. M., & Lovenduski, N. S. (2016). Mapping the Antarctic Polar Front: Weekly realizations from 2002 to 2014. *Earth System Science Data*, *8*, 191–198. https://doi.org/10.5194/essd-8-191-2016

Freeman, N. M., Lovenduski, N. S., & Gent, P. R. (2016). Temporal variability in the Antarctic Polar Front (2002–2014). *Journal of Geophysical Research: Oceans*, *121*, 7263–7276. https://doi.org/10.1002/2016JC012145

Frey, W. R., & Kay, J. E. (2018). The influence of extratropical cloud phase and amount feedbacks on climate sensitivity. *Climate Dynamics*, *50*, 3097–3116. https://doi.org/10.1007/s00382-017-3796-5

Griggs, D. J., & Choularton, T. W. (1986). A laboratory study of secondary ice particle production by the fragmentation of rime and vapour-grown ice crystals. *Quarterly Journal of the Royal Meteorological Society*, *112*, 149–163. https://doi.org/10.1002/qj.49711247109

Gunn, R., & Kinzer, G. D. (1949). The terminal velocity of fall for water droplets in stagnant air. *Journal of Meteorology*, *6*, 243–248. https://doi.org/10.1175/1520-0469(1949)006<0243:ttvoff>2.0.co;2

Haarig, M., Ansmann, A., Gastelger, J., Kandler, K., Althausen, D., Baars, H., et al. (2017). Dry versus wet marine particle optical properties: RH dependence of depolarization ratio, backscatter, and extinction from multiwavelength lidar measurements during SALTRACE. *Atmospheric Chemistry and Physics*, *17*(23), 14199–14217. https://doi.org/10.5194/acp-17-14199-2017

Hallet, J., & Mossop, S. C. (1974). Production of secondary ice particles during the riming process. *Nature*, *249*, 26–28. https://doi.org/10.1038/249026a0

Hogan, R. J., & Westbrook, C. D. (2014). Equation for the microwave backscatter cross section of aggregate snowflakes using the self-similar Rayleigh-Gans approximation. *Journal of the Atmospheric Sciences*, *71*, 3292–3301. https://doi.org/10.1175/jas-d-13-0347.1

Hu, Y., Vaughn, M., Lin, B., Yang, P., Flittner, D., Hunt, B., et al. (2007). The depolarization-attenuated backscatter relation: CALIPSO lidar measurement vs. theory. *Optics Express*, *15*, 5327–5332. https://doi.org/10.1364/oe.15.005327

Hu, Y., Winker, D., Vaughan, M., Lin, B., Omar, A., Trepte, C., et al. (2009). CALIPSO/CALIOP cloud phase discrimination algorithm. *Journal of Atmospheric and Oceanic Technology*, *26*, 2293–2309. https://doi.org/10.1175/2009JTECHA1280.1

Huang, Y., Chubb, T., Baumgardner, D., deHoog, M., Siems, S. T., & Manton, M. J. (2017). Evidence for secondary ice production in Southern Ocean open cellular convection. *Quarterly Journal of the Royal Meteorological Society*, *143*(704), 1685–1703. https://doi.org/10.1002/qj.3041

Huang, Y., Siems, S. T., & Manton, M. J. (2021). Wintertime in situ cloud microphysical properties of mixed-phase clouds over the Southern Ocean. *Journal of Geophysical Research: Atmospheres*, *126*(11), e2021JD034832. https://doi.org/10.1029/2021jd034832

Hurrell, J. W., Holland, M. M., Gent, P. R., Ghan, S., Kay, J. E., Kushner, P. J., et al. (2013). The Community Earth System Model: A framework for collaborative research. *Bulletin of the American Meteorological Society*, *94*, 1339–1360. https://doi.org/10.1175/bams-d-12-00121.1

Illingworth, A. J., Barker, H. W., Beljaars, A., Ceccaldi, M., Chepfer, H., Clerbaux, N., et al. (2015). The EarthCARE satellite: The next step forward in global measurements of clouds, aerosols, precipitation, and radiation. *Bulletin of the American Meteorological Society*, *96*(8), 1311–1332. https://doi.org/10.1175/bams-d-12-00227.1

Josset, D., Rogers, R., Pelon, J., Hu, Y., Liu, Z., Omar, A., & Zhai, P.-W. (2011). CALIPSO lidar ratio retrieval over the ocean. *Optics Express*, *19*, 18696–18706. https://doi.org/10.1364/oe.19.018696

Kay, J. E., Wall, C., Yettella, V., Medeiros, B., Hannay, C., Caldwell, P., & Bitz, C. (2016). Global climate impacts of fixing the southern ocean shortwave radiation bias in the Community Earth System Model (CESM). *Journal of Climate*, *29*, 4617–4636. https://doi.org/10.1175/jcli-d-15-0358.1

Keinert, A., Spannagel, D., Leisner, T., & Kiselev, A. (2020). Secondary ice production upon freezing of freely falling drizzle drops. *Journal of the Atmospheric Sciences*, *77*, 2959–2967. https://doi.org/10.1175/JAS-D-20-0081.1

Koenig, L. R. (1963). The glaciating behavior of small cumulonimbus clouds. *Journal of the Atmospheric Sciences*, *20*, 29–47. https://doi.org/10.1175/1520-0469(1963)020<0029:tgbosc>2.0.co;2

Korolev, A., & Leisner, T. (2020). Review of experimental studies of secondary ice production. *Atmospheric Chemistry and Physics*, *20*, 11767–11797. https://doi.org/10.5194/acp-20-11767-2020

Lancaster, H. O. (1961). Significance tests in discrete distributions. *Journal of the American Statistical Association*, *56*, 223–234. https://doi.org/10.1080/01621459.1961.10482105

Lasher-Trapp, S., Leon, D. C., DeMott, P. J., Villanueva-Birriel, C. M., Johnson, A. V., Moser, D. H., et al. (2016). A multisensory investigation of rime splintering in tropical maritime cumuli. *Journal of the Atmospheric Sciences*, *73*, 2547–2564. https://doi.org/10.1175/JAS-D-15-0285.1

Lauber, A., Kiselev, A., Pander, T., Handmann, P., & Leisner, T. (2018). Secondary ice formation during freezing of levitated droplets. *Journal of the Atmospheric Sciences*, *75*, 2815–2826. https://doi.org/10.1175/JAS-D-18-0052.1

Lawson, R. P., Woods, S., & Morrison, H. (2015). The microphysics of ice and precipitation development in tropical cumulus clouds. *Journal of the Atmospheric Sciences*, *72*, 2429–2445. https://doi.org/10.1175/JAS-D-14-0274.1

Liu, J., Xiao, T., & Chen, L. (2011). Intercomparison of air-sea heat fluxes over the Southern Ocean. *Journal of Climate*, *24*, 1198–1211. https://doi.org/10.1175/2010JCLI3699.1

Liu, W., Lu, J., Xie, S.-P., & Fedorov, A. (2018). Southern Ocean heat uptake, redistribution, and storage in a warming climate: The role of meridional overturning circulation. *Journal of Climate*, *31*, 4727–4743. https://doi.org/10.1175/JCLI-D-17-0761.1

Liu, Y., Geerts, B., Miller, M., Daum, P., & McGraw, R. (2008). Threshold radar reflectivity for drizzling clouds. *Geophysical Research Letters*, *35*, L03807. https://doi.org/10.1029/2007GL031201

Mace, G. G., Benson, S., & Hu, Y. (2020). On the frequency of occurrence of the ice phase in supercooled Southern Ocean low clouds derived from CALIPSO and CloudSat. *Geophysical Research Letters*, *47*, e2020GL087554. https://doi.org/10.1029/2020GL087554

Mace, G. G., & Protat, A. (2018). Clouds of the the Southern Ocean from the RV Investigator during CAPRICORN. Part 2: The properties of non precipitating stratocumulus. *Journal of Applied Meteorology and Climatology*, *57*, 1805–1823. https://doi.org/10.1175/JAMC-D-17-0195.1

Mace, G. G., Protat, A., Humphries, R. S., Alexander, S. P., McRobert, I. M., Ward, J., et al. (2021). Southern Ocean cloud properties derived from CAPRICORN and MARCUS data. *Journal of Geophysical Research: Atmospheres*, *126*, e2020JD033368. https://doi.org/10.1029/2020JD033368

Mace, G. G., & Zhang, Q. (2014). The CloudSat radar-lidar geometrical profile product (RL-GeoProf): Updates, improvements, and selected results. *Journal of Geophysical Research*, *119*, 9441–9462. https://doi.org/10.1002/2013JD021374

Marchand, R., Mace, G. G., Ackerman, T., & Stephens, G. (2008). Hydrometeor detection using CloudSat—An Earth-orbiting 94 GHz cloud radar. *Journal of Atmospheric and Oceanic Technology*, *25*, 519–533. https://doi.org/10.1175/2007jtecha1006.1

Marshall, J., & Speer, K. (2012). Closure of the meridional overturning circulation through Southern Ocean upwelling. *Nature Geoscience*, *5*, 171–180. https://doi.org/10.1038/NGEO1391

Matrosov, S. Y., Shupe, M. D., & Djalalova, I. V. (2007). Snowfall retrievals using millimeter-wavelength cloud radars. *Journal of Applied Meteorology*, *47*, 769–777. https://doi.org/10.1175/2007JAMC1768.1

McCluskey, C. S., Hill, T. C. J., Humphries, R. S., Rauker, A. M., Moreau, S., Strutton, P. G., et al. (2018). Observations of ice nucleating particles over Southern Ocean waters. *Geophysical Research Letters*, *45*(11), 989–997. https://doi.org/10.1029/2018GL079981

McFarquhar, G. M., Bretherton, C. S., Marchand, R., Protat, A., DeMott, P. J., Alexander, S. P., et al. (2021). Observations of clouds, aerosols, precipitation, and surface radiation over the Southern Ocean: An overview of CAPRICORN, MARCUS, MICRE, and SOCRATES. *Bulletin of the American Meteorological Society*, *102*(4), E894–E928. https://doi.org/10.1175/BAMS-D-20-0132.1

Meyers, M. P., DeMott, P. J., & Cotton, W. R. (1992). New primary ice-nucleation parameterizations in an explicit cloud model. *Journal of Applied Meteorology*, *31*, 708–721. https://doi.org/10.1175/1520-0450(1992)031<0708:npinpi>2.0.co;2

Milbrandt, J., & Yau, M. (2005). A multimoment bulk microphysics parameterization. Part I: Analysis of the role of the spectral shape parameter. *Journal of the Atmospheric Sciences*, *62*(9), 3051–3064. https://doi.org/10.1175/jas3534.1

Mitchell, D. L. (1996). Use of mass- and area-dimensional power laws for determining precipitation particle terminal velocities. *Journal of the Atmospheric Sciences*, *53*, 1710–1723. https://doi.org/10.1175/1520-0469(1996)053<1710:uomaad>2.0.co;2

Mitchell, D. L., & Heymsfield, A. J. (2005). Refinements in the treatment of ice particle terminal velocities, highlighting aggregates. *Journal of the Atmospheric Sciences*, *62*(5), 1637–1644. https://doi.org/10.1175/jas3413.1

Mossop, S. C. (1986). The origin and concentration of ice crystals in clouds. *Bulletin of the American Meteorological Society*, *66*(3), 264–273.

Mossop, S. C., Ono, A., & Wishart, E. R. (1970). Ice particles in maritime clouds near Tasmania. *Quarterly Journal of the Royal Meteorological Society*, *96*, 487–508. https://doi.org/10.1002/qj.49709640910

Naud, C. M., Booth, J. F., & Del Genio, A. D. (2014). Evaluation of ERA-Interim and MERRA cloudiness in the Southern Ocean. *Journal of Climate*, *27*, 2109–2124. https://doi.org/10.1175/JCLI-D-13-00432.1

Ono, A., Kobayashi, F., & Sugaya, H. (1972). Evidence on the nature of ice crystal multiplication processes in natural cloud. *Journal de Recherches Atmospheriques*, *6*, 399–402. https://doi.org/10.1109/tmag.1972.1067514

Platt, C. M. R. (1977). Lidar observations of a mixed-phase altostratus cloud. *Journal of Applied Meteorology*, *16*, 339–345. https://doi.org/10.1175/1520-0450(1977)016<0339:looamp>2.0.co;2

Posselt, D., & Mace, G. (2014). The influence of parameter uncertainty on snowfall retrievals using Markov Chain Monte Carlo solution methods. *Journal of Applied Meteorology and Climatology*, *53*, 2034–2057.

Protat, A., Schulz, E., Rikus, L., Sun, Z., Xiao, Y., & Keywood, M. (2017). Shipborne observations of the radiative effect of Southern Ocean Clouds. *Journal of Geophysical Research: Atmospheres*, *122*, 318–328. https://doi.org/10.1002/2016jd026061

Pruppacher, H. R., & Klett, J. D. (1997). *Microphysics of clouds and precipitation* (p. 954). Kluwer Academic Publishers.

Royer, P., Bizard, A., Sauvage, L., & Thobois, L. (2014). *Validation protocol and intercomparison campaigns with the R-MAN 510 aerosol lidar*. https://doi.org/10.13140/2.1.4778.1767

Sassen, K., Zhao, H., & Dodd, G. C. (1992). Simulated polarization diversity lidar returns from water and precipitating mixed phase clouds. *Applied Optics*, *31*(15), 2914–2923. https://doi.org/10.1364/ao.31.002914

Schneider, D. P., Kay, J. E., & Lenaerts, J. (2020). Improved clouds over Southern Ocean amplify Antarctic precipitation response to ozone depletion in an earth system model. *Climate Dynamics*, *55*, 1665–1684. https://doi.org/10.1007/s00382-020-05346-8

Schneider, D. P., & Reusch, D. B. (2015). Antarctic and Southern Ocean surface temperature in CMIP5 models in the context of the surface energy budget. *Journal of Climate*, *29*, 1689–1716. https://doi.org/10.1175/JCLI-D-15-0429.1

Silber, I., Fridlind, A. M., Verlinde, J., Ackerman, A. S., Chen, Y.-S., Bromwich, D. H., et al. (2019). Persistent supercooled drizzle at temperatures below −25°C observed at McMurdo Station, Antarctica. *Journal of Geophysical Research: Atmospheres*, *124*, 10878–10895. https://doi.org/10.1029/2019JD030882

Sokolov, S., & Rintoul, S. R. (2009). Circumpolar structure and distribution of the Antarctic Circumpolar Current fronts: 1. Mean circumpolar paths. *Journal of Geophysical Research*, *114*, C11018. https://doi.org/10.1029/2008JC005108

Stephens, G. L., Vane, D. G., Tanelli, S., Im, E., Durden, S., Rokey, M., et al. (2008). CloudSat mission: Performance and early science after the first year of operation. *Journal of Geophysical Research*, *113*, D00A18. https://doi.org/10.1029/2008JD009982

Sullivan, S. C., Hoose, C., Kiselev, A., Leisner, T., & Nenes, A. (2018). Initiation of secondary ice production in clouds. *Atmospheric Chemistry and Physics*, *18*, 1593–1610. https://doi.org/10.5194/acp-18-1593-2018

Sullivan, S. C., Hoose, C., & Nenes, A. (2017). Investigating the contribution of secondary ice production to in-cloud crystal numbers. *Journal of Geophysical Research: Atmospheres*, *122*, 9391–9412. https://doi.org/10.1002/2017JD026546

Trenberth, K. E., & Fasullo, J. T. (2010). Simulation of present-day and twenty-first-century energy budgets of the Southern Oceans. *Journal of Climate*, *23*, 440–454. https://doi.org/10.1175/2009JCLI3152.1

Vardiman, L. (1978). The generation of secondary ice particles in clouds by crystal-crystal collision. *Journal of the Atmospheric Sciences*, *35*, 2168–2180. https://doi.org/10.1175/1520-0469(1978)035<2168:tgosip>2.0.co;2

Varma, V., Morgenstarn, O., Field, P., Furtado, K., Williams, J. P. H., & Hyder, P. (2020). Improving the Southern Ocean cloud albedo biases in a general circulation model. *Atmospheric Chemistry and Physics*, *20*, 7741–7751. https://doi.org/10.5194/acp-20-7741-2020

Vergara-Temprado, J., Miltenberger, A. K., Furtado, K., Grosveno, D. P., Shipway, B. J., Hill, A. A., et al. (2018). Strong control of Southern Ocean cloud reflectivity by ice nucleating particles. *Proceedings of the National Academy of Sciences*, *115*, 2687–2692. https://doi.org/10.1073/pnas.1721627115

Wegener, A. (1911). *Thermodynamik der atmosphäre* (p. 331). J.A. Barth Leipzig.

Winker, D. M., Vaughan, M. A., Omar, A., Hu, Y., Powell, K. A., Liu, Z., et al. (2009). Overview of the CALIPSO Mission and CALIOP data processing algorithms. *Journal of Atmospheric and Oceanic Technology*, *26*, 2310–2323. https://doi.org/10.1175/2009JTechA1281.1